

# Surrogate spacer grid design for fluid-structure interactions studies in fuel bundles

Noah A. Weichselbaum, Shadman Hussain, Pierre Korysko, Morteza Rahimi-Abkenar, Philippe M. Bardet, and Majid T. Manzari

The George Washington University  
Washington, DC 20052  
weichselbaum@gwu.edu

## ABSTRACT

To experimentally study the dynamic response of fuel assemblies during LOCA and seismic events, a surrogate fuel bundle is designed and built with generic spacer grids. The spacer grids have the main characteristics of prototypical grids and aim to reproduce some of their main dynamic characteristics. To allow controlling the contact between springs and rods, a bi-metallic spacer grid design is selected. Such a design has the added benefit of enabling minimization of uncertainties on contact force between spring and rod. Details of the design and fabrication are reported. Structural response of an externally excited surrogate fuel bundle is presented to illustrate the bundle behavior. Data enable identifying the effects of springs and dimples on bundle dynamics and provide validation test cases for finite element analysis.

## KEYWORDS

PWR Fuel Assembly, Fluid Structure Interaction, Particle Image Velocimetry, Digital Image Correlation

## 1. INTRODUCTION

A Pressurized Water Reactor (PWR) fuel assembly is composed of an array of fuel rods with spacer grids located axially along the height of the assembly maintaining the rods in a constant pitch to diameter ratio ( $P/D$ ). In a spacer grid cell, each individual rod is held in place by two orthogonal sets of one spring facing two dimples. Spacer grid designs tend to be proprietary and limited information is openly available on their detailed geometry, such as the spring profile and associated spring constant. This limited information makes it challenging to validate high-fidelity computational fluid dynamics (CFD) tools applied to these geometries.

For experiments with fuel bundles, having a spacer grid that is close to the product used in industry can be important, in fact, groups utilize spacer grids supplied directly by manufacturers to resolve flow field inside the bundle [1,2]. In one study button type springs are utilized to accommodate surrogate rod dimensions [10]. In these experimental studies, turbulent flow downstream of the spacer grid has been characterized with PIV, which is a non-intrusive optical measurement technique that provides full field velocity data. In cases where flow induced vibration and surrogate materials are employed, it is primordial to properly scale the surrogate spring contact force to the rod to guarantee that characteristic effects are captured in the experimental facility.

For seismic and large break loss of coolant accident (LOCA) studies on fuel bundles near prototypical operating conditions, there exists limited information on the fluid and structure coupled response. It is

therefore beneficial to deploy full field fluid structure interaction (FSI) diagnostics of the rod bundle deflections coupled with the surrounding turbulent flow. This can be accomplished in an index matched environment with transparent fuel rods. Here, PIV captures the velocity field within the bundle, while simultaneously digital image correlation (DIC) tracks the overall bundle displacements [3], thus data necessary for understanding the FSI coupling are captured.

One working fluid that has been used in a number of experimental facilities is Para-cymene [4,5]. This fluid has a low kinematic viscosity ( $\nu = 0.846 \times 10^{-6} \text{ m}^2/\text{s}$ ) that is conducive to reaching high Reynolds number flows and has an index of refraction close to several optically transparent materials ( $n_D = 1.4875$ ). The index matching can be further refined with use of temperature controlled binary mixtures [6]. Several materials that can be matched with Para-cymene near room temperature are acrylic, pyrex, and BK-7 glass. These materials can be scaled to have similar resonant characteristics as prototype fuel rods composed of Zircaloy tubes with uranium dioxide pellets [7].

In this study, acrylic ( $n_D = 1.4912$ ) is selected as the surrogate rod material, Fig. 1. To match both resonant characteristics and dimensionless properties associated with the fluid, solid acrylic rods with a diameter 50% larger than typical prototypical rods are used, necessitating a scaled spacer grid to accommodate both the increased diameter rods and different material properties. A non-mixing vane design spacer grid from the PSBT benchmark [8] is used as the basis of the design for the scaled spacer grid with a  $P/D$  of 1.33, Fig. 2. All dimensions are scaled by a factor of 1.5 to accommodate for the increased rod diameter, and from the PSBT benchmarks tests it appeared that both the springs and dimples are embossed directly from the spacer grid wall. An analytical analysis and finite element analysis (FEA) has been conducted on this spring geometry, and it was found that the spring stiffness is disproportionately high when compared with published values [9]. To address this issue, new spring designs have been considered that provide the asymmetric supports indicative of the spring and dimple, which for studies on bundle oscillations are significant for the dynamic response of the bundle. Therefore it was determined that a scaled spacer grid is needed that properly models the spring and dimple interface with the fuel rod.

This paper is organized as follows. In section 2 the scaling and design of the spacer grid design is presented. Section 3 describes a FEA of the spring. In section 4 the actual manufacturing process of the new spacer grids is discussed along with the integration into the experimental facility. The last section presents results for the integration of the spacer grids into a refractive index matched facility for studies of fuel rod bundles under loading typically encountered during seismic or large break LOCA events.

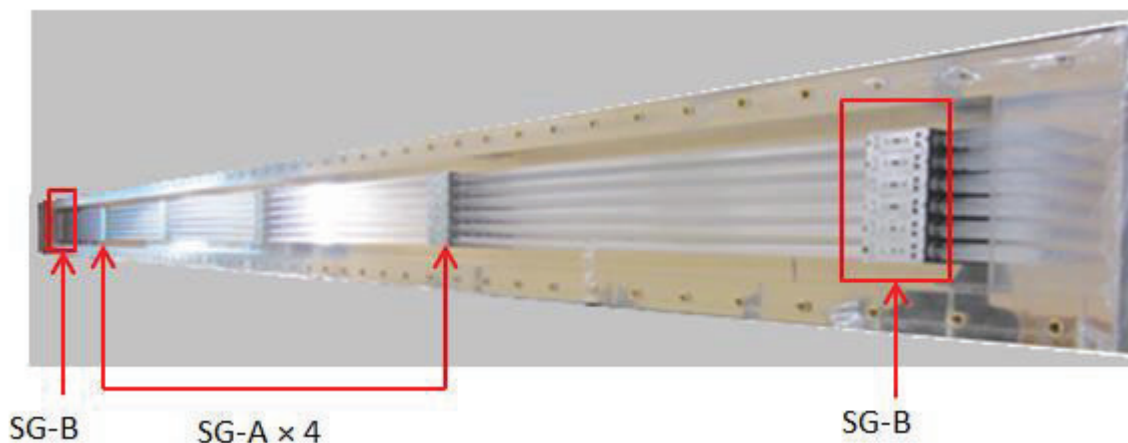


**Figure 1. Final Rod Bundle. End spacer grids (SG-B) are rigidly fixed to the test section, while the four center one (SG-A) are free to deflect.**

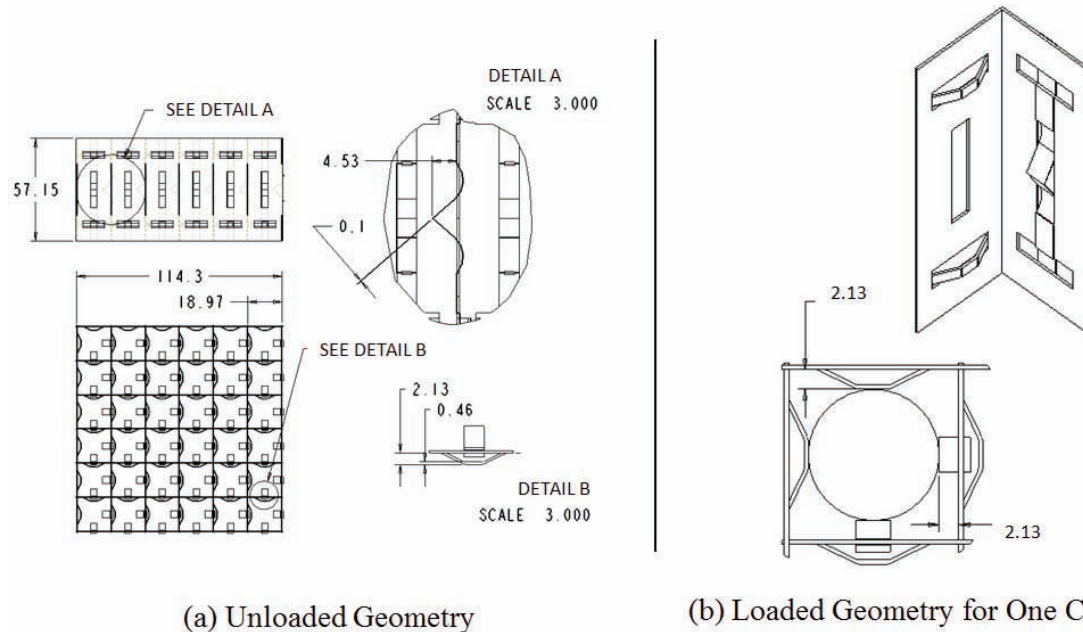


Figure 2. Scaled Spacer Grid Geometry for spacer grid A, reported dimensions are in units of mm.

## 2. DESIGN OF A SPACER GRID FOR SURROGATE MATERIALS

### 2.1 Scaling for surrogate materials

The current design utilizes geometry from a non-mixing vane spacer grid that was used in a study on subchannel flow for the PSBT benchmark test [8], but is increased by 50% to ensure proper scaling of bundle natural frequency. However, the spring design is modified, while maintaining the other proportions to ensure an appropriate  $P/D$ , flow area, and pressure drop through the grid. The  $P/D$  is 1.33, and the flow area per cell is  $180 \text{ mm}^2$  with a pressure drop across the grid estimated with the deStordeur model as  $3.13 \times 10^3 \text{ Pa}$  and with the Rehme model as  $1.63 \times 10^3 \text{ Pa}$  for a Reynolds number of  $1.0 \times 10^5$  [11].

Comparing the spring from Fig. 2 with that from the PSBT benchmark test, the primary difference is that a bi-metallic spring design is utilized where the geometry and the material are changed. The justification for these changes, is due to the difference in weight and diameter of the surrogate material for the fuel rod being used, Table 1, with more details on the design to follow.

Table I. Fuel Bundle Parameters

	Fuel Rod			Spacer Grids	Rod section Weight in Air (N)	Spring Contact Force (N)	Non Dim. Force	Spring Stiffness (N/mm)	Dimple Stiffness (N/mm)
	do (m)	di (m)	L (m)						
<b>Prototype</b>	0.0095	0.008	4	8	3.484	25 [12]	5.62	152.9 [9]	8840 [9]
<b>Model</b>	0.0143	n/a	4	6	1.386	9.8	5.62	4.2	4030

A full height  $6 \times 6$  rod bundle is utilized for the fuel assembly model, this helps to maintain similar resonant characteristics to a reduced order  $6 \times 6$  bundle of Zircaloy rods with  $\text{UO}_2$  pellets which is described in more detail in Weichselbaum et al. 2014 [7]. A total of 6 spacer grids are selected for the bundle. The four intermediate grids are SG-A type, Fig. 1, and these are free to deflect during testing. The end spacer grids are rigidly fixed to the wall of the test section and have stronger springs to prevent eventual drop of a rod during bundle excitation. These grids are labeled SG-B. This spacer grid configuration is modeled after a prototypical PWR fuel assembly where Inconel spacer grids are used at top and bottom due to the materials high strength and corrosion resistance, while Zircaloy spacer grid are used in the intermediary because of its better neutron economy [15]. The material properties for the two types of spacer grids used in this facility can be seen in Table II.

**Table II. Model Spacer Grid Properties**

	Strap			Spring		
	Material	Thickness (m)	Surface Roughness (m)	Material	Thickness (m)	Surface Roughness $R_a$ (m)
<b>SG-A</b>	26 AWG 304 Stainless Steel	$4.6 \times 10^{-4}$	$8 \times 10^{-7}$	Spring Tempered 301 Stainless Steel	$1.02 \times 10^{-4}$	$4 \times 10^{-7}$
<b>SG-B</b>	25 AWG 304 Stainless Steel	$5.3 \times 10^{-4}$	$8 \times 10^{-7}$		$2.03 \times 10^{-4}$	$4 \times 10^{-7}$

The pertinent information for the design of the spacer grids is the geometry and material for the fuel rods, as well as the number of grids utilized for the model. With this information, it is possible to determine a dimensionless contact force to properly model the spring of SG-A. Per fuel rod, each pair of springs in a spacer grid has to be able to hold the weight of the unsupported span of the rod between grids in air. Typically fuel assemblies are designed with a spring contact force that enables the bundle to withstand loads during shipping and installation into the reactor, which leads to a contact force of about 25 N [12]. The dimensionless contact force is the ratio of the weight of the unsupported rod span between grids in air, to the normal force that is a product of the spring contact force and coefficient of friction. For the model parameters, to match the dimensionless contact force, the spring contact force is 9.80 N.

A spring was initially designed that maintained both this scaled contact force and a scaled spring constant based on a published value of 153 N/mm [9]. The deflection of this scaled spring when the rod is placed in contact is at the sub-millimeter scale. During the design of the model rod bundle, it became apparent that this small a deflection would lead to high uncertainty in the spring contact force. Therefore to produce a spring with an appropriate contact force and acceptable uncertainty level, the scaled spring constant could not be maintained.

## 2.2 Uncertainty analysis for spring design

A geometrical model of a rod in a spacer grid cell is used to predict analytically the overall uncertainty,  $u_F$ , on contact force,  $F = kx$ , see Fig. 3 for the model. The latter is due to uncertainties both in spring displacement and stiffness,  $u_x$  and  $u_k$ , respectively. This enables optimization of the spacer grid and spring design to minimize uncertainty on contact force in static environment. The methodology takes into account tolerances of each manufacturing process, which are summarized in Table III.

**Table III. Tolerances for manufacturing of spacer grid strap.  $u_i$  are identical for SG-A & B**

	<b>Rod Diameter</b> [ $u_d$ ]	<b>Thickness of strap</b> [ $u_t$ ]	<b>Laser Welding</b> [ $u_{lw}$ ]	<b>Laser Cutting</b> [ $u_{lc}$ ]	<b>Embossed Features</b> [ $u_e$ ]
<b>manufacturing Uncertainty (m)</b>	$2.54 \times 10^{-4}$	$3.81 \times 10^{-5}$	$2.03 \times 10^{-4}$	$2.03 \times 10^{-4}$	$3.81 \times 10^{-4}$
<b>Measured uncertainty (m)</b>		$1.0 \times 10^{-5}$	$1.3 \times 10^{-4}$	$2.0 \times 10^{-4}$	$1.1 \times 10^{-4}$

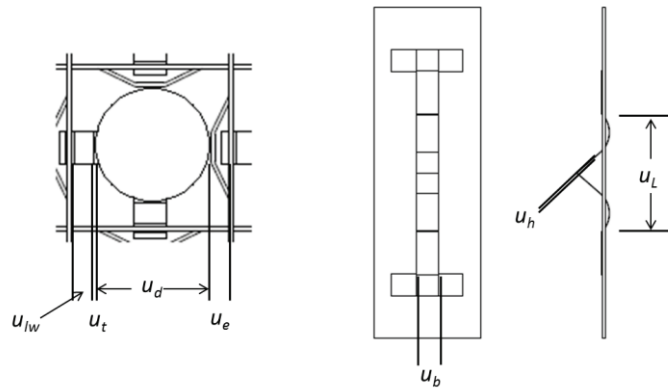


**Figure 3. Uncertainty values applied to model geometry**

For a process  $y$  with an analytical relation  $f(x_i)$  relating it to its input variables,  $x_i$ :

$$y = f(x_i), \quad (1)$$

the design stage uncertainty is [13]:

$$u_c(y) = \sqrt{\sum_i \left( \frac{\partial f}{\partial x_i} u_{x_i} \right)^2} \quad (2)$$

The uncertainty in the spring initial displacement is based on the absolute tolerances of the manufacturing processes and materials which are fixed, Fig. 3 and eq. 3. In order to keep this uncertainty value in the same order of magnitude as the uncertainty in the spring stiffness, the displacement needs to be in the millimeter scale and a value of 2.3 mm is selected.

$$u_x = \sqrt{u_d^2 + u_t^2 + u_{lw}^2 + u_e^2} \quad (3)$$

With data reported in Table III, the uncertainty on initial displacement for an initial displacement of 2.3 mm is 21.5% based on tolerances. However, once received the straps have been carefully measured, and the tolerance on the fabricated grids are reported in the last row of table III. With these values the uncertainty on initial spring compression is 13.1%.

For the spring stiffness more flexibility is introduced in minimizing the uncertainty as the stiffness is estimated with the Euler Bernoulli Beam theory for a rectangular beam clamped at both ends with a concentrated load at its center [14]. It is therefore possible to optimally select its materials (and therefore Young's modulus,  $E$ ), its thickness,  $h$ , width,  $b$ , and length,  $L$ . Here a spring tempered thin gauge stainless steel is selected for the springs and the uncertainty on Young's modulus is neglected. Based on eq. 2, the overall uncertainty on spring stiffness reduces to:

$$u_k = k \sqrt{\left(\frac{u_b}{b}\right)^2 + \left(3 \frac{u_h}{h}\right)^2 + \left(-3 \frac{u_L}{L}\right)^2} \quad (4)$$

With current materials and manufacturing tolerance reported in table III,  $u_k$  is 27.3%. With the measured uncertainties for stiffness,  $u_k$  is 1.0%, and the overall uncertainty on contact force is the root of the sum of the square (RSS) of  $u_x$  and  $u_k$  and is 13.2%.

The uncertainties with a spring displacement of 2.3 mm are tabulated in Table IV for SG-A grids utilized in the experimental facility that has the dimensional contact force stipulated in Table I.

**Table IV. Calculated Relative Uncertainties**

Spring Parameters				Measured Uncertainty (m)		
<b>b (mm)</b>	<b>h (mm)</b>	<b>L (mm)</b>	<b>E (Pa)</b>	$u_b$	$u_h$	$u_L$
1.91	0.457	20.2	$1.93 \times 10^{11}$	$2.0 \times 10^{-5}$	$1.0 \times 10^{-5}$	$2.0 \times 10^{-5}$

The second type of spacer grid (SG-B) has a contact force that is three times higher, and is made with both thicker gauge straps and springs, the values of which are reported in table II. The relative uncertainty on contact force in these grids is 13.2% as well.

### 3. CHARACTERIZATION OF SPRING ELEMENT

#### 3.1 Analytical analysis

The uncertainty analysis for SG-A defined the distance the spring needs to deflect from the unloaded position, prior to when the fuel rod is inserted, to the final position with the fuel rod in place, this forces use of a spacer grid with bimetallic springs. This feature was taken advantage of to design springs that have constant spring stiffness over the whole allowable displacement. This leads to a linear contact force, which simplifies simulations of this system and is different than prototypical grids, where the spring stiffness strongly depends on deformation. To estimate the rod deflection from a unit load (ie. 1 N), first an analytical analysis utilizing the Euler Bernoulli Beam theory described above is employed. However, while this methodology is acceptable to estimate design stage uncertainty, it does not provide adequate confidence to estimate the actual contact force. Thus a finite element analysis is performed.

#### 3.2 Finite element analysis

The FEA is conducted in ANSYS R15.0. The geometry for the spring from Fig. 2 can be seen in Fig. 4 with the associated boundary conditions from the grid strap, which is assumed rigid.

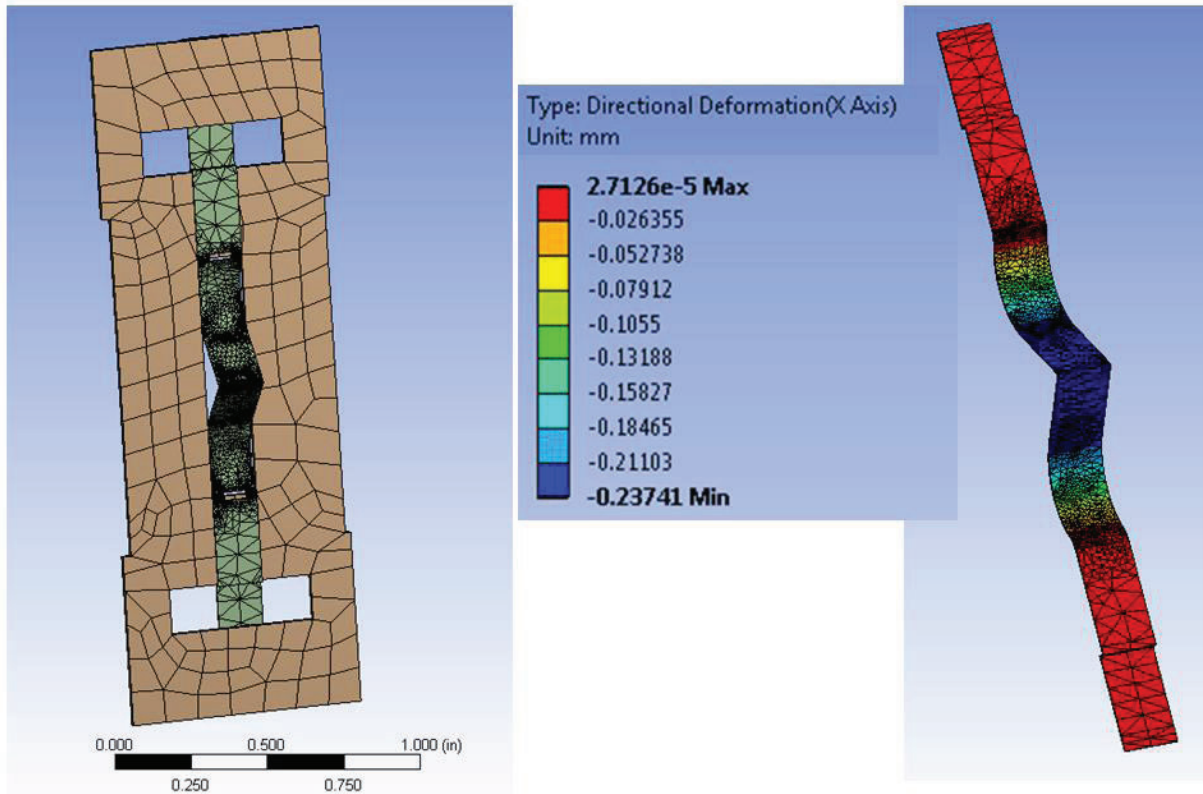


**Figure 4. FEA boundary conditions and results for unit load analysis with strap geometry hidden for display purposes**

For the first analysis material properties for spring tempered stainless steel are defined, Table V, and a unit load is applied at the point where the fuel rod is in contact with the spring, Fig. 4.

**Table V. Material Properties for Spring Tempered Stainless Steel**

$\rho$ (kg/m <sup>3</sup> )	Poisson Ratio	E (Pa)	Tensile Strength (Pa)	Yield Strength (Pa)
7,880	0.457	$1.93 \times 10^{11}$	$1.86 \times 10^9$	$1.55 \times 10^9$

The analysis is conducted with an iterative method in which a 5% allowable change is stipulated for the deformation of the spring. A coarse mesh is used in the first analysis, and locations that are identified as being pertinent to the analysis are refined for the ensuing steps. For the unit load analysis, five iterations with a maximum node count of 44309 are required to reach the specified criteria for deformation, with a max deformation at the center of the spring of 0.237 mm, Fig. 4. This value is less than that predicted with the analytical analysis, but is at the same order of magnitude which lends confidence to the FEA analysis. The spring constant can then be determined from  $F = kx$  to be 4.2 N/mm.

With the spring constant defined, the contact force can be determined for the deflection of the spring when the rod is inserted which is designed to be 2.33 mm. At this deflection, the contact force is 9.8 N. To ensure the spring will not experience plastic deformation if the rod vibrations cause the spring to deflect past the designed distance, a second set of analyses are conducted in ANSYS. A prescribed displacement is utilized in place of the unit load in this set of simulations. The maximum distance the

spring can deflect is 4.52 mm, which is the distance if the spring is deformed all the way against the strap. Five points are analyzed between the loaded spring displacement value and the maximum deflection, Fig. 5.

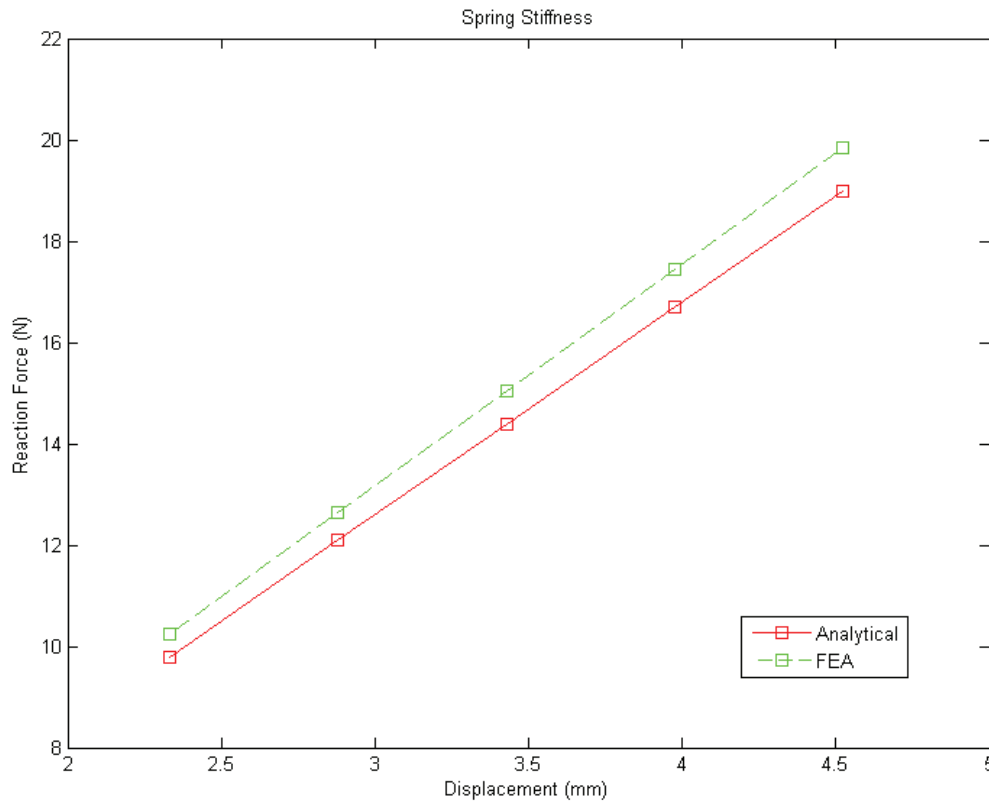


**Figure 5. Contact force vs. displacement for both calculated and FEA results for SG-A**

The contact force is found to have a linear relationship within the possible displacement values for the spring within the spacer grid ensuring they will not plastically deform during testing and spring stiffness of 4.2 N/mm. The maximum von-Mises stress is found to be of 1.35 GPa at the maximum allowable displacement which is 20% less than the yield stress of the material.

#### **4. SCALED SPACER GRID MANUFACTURING AND INTEGRATION INTO FACILITY**

With the geometry of the spacer grid defined from sections 2 through 3, the final grids are modeled in 3D computer aided drawing software Pro Engineer, Fig. 6 (which can be provided to groups interested in modeling the bundle or fabricating their own spacer grids). From this assembly a top down set of drawings of all of the individual components is created. These detailed drawings are then provided to a group of specialized manufacturing firms. One group laser cuts the grid straps from 25 or 26 AWG stainless steel, depending on grid type, in addition to the respective springs from spring tempered stainless steel. This same group then forms the dimples from the grid straps with one custom set of dies, and forms the springs from the spring tempered steel with another custom set of dies. The tolerances for these machining processes are reported in Table III. One notable feature of these spacer grids is that all the springs are installed on the same side of a strap, Fig. 2, while for typical bundles, they are alternated. This will have consequences on elucidating sources of damping in bundle dynamics as briefly shown hereafter.

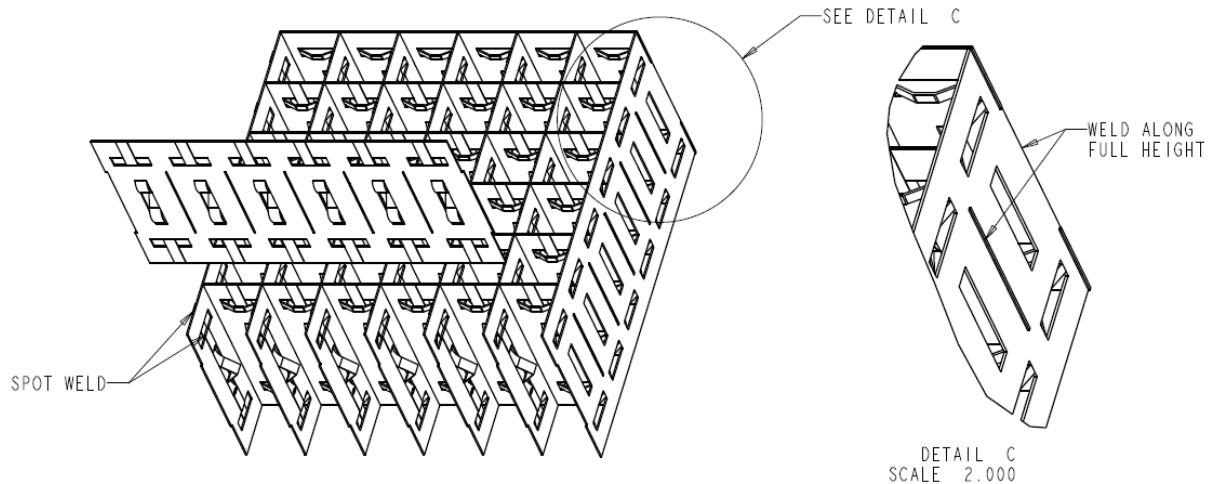


**Figure 6. Assembly view of spacer grid**

The formed grid straps and springs are then assembled into their final form in house inside a special frame to guarantee alignment of the straps, and then are sent to a second firm to have precision laser welding applied, Fig. 6. The grid straps on the interior of the spacer grid fit together in an egg-crate fashion, and then the outer walls are fitted onto this base structure. In this manner, the majority of the laser welding for the straps are on the exterior of the structure. The four corners are welded along the entire edge, and then the protrusion from the interior straps through the outer strap walls are laser welded as well. To fix the openings for the interior straps, laser spot welds are placed at every intersection on both the top and bottom of the grid, where the laser spot welds diameter are no larger than the thickness of the strap material to prevent blockages to the axial flow. The springs are also laser welded into place with spot welds placed where the spring enters the cavity in the strap wall and at the extremities of the spring, which are flush with the top and bottom of the spacer grid, respectively. The same group then applies a laser engraved pattern on the four exterior surfaces of the spacer grid that are used for reconstructing the bundle displacement with DIC as described in Section 5.

Acrylic rods are then inserted into the spacer grids, with the completed surrogate fuel assembly being comprised of 36 acrylic rods and 6 spacer grids, Fig. 1. This fuel assembly is then mounted in an acrylic channel to allow for axial flow through the bundle, and as indicated previously the two SG-B are rigidly fixed to the acrylic channel to hold the bundle in place with hydrofoils to minimize disturbance to the flow, Fig. 7. This inner acrylic channel is surrounded by a secondary acrylic tank to provide a low pressure boundary, and both are mounted on a stainless steel inlet plenum that is outfitted with flow conditioning elements to provide a uniform initial flow into the test section. This entire structure is mounted on a shake table that is a 3 × 3 m square platform with six degrees of freedom, Fig. 7.

This facility allows for testing the fuel assembly at near prototypical conditions with a fluid velocity of up to 6 m/s within the fuel bundle provided by two 50 Hp centrifugal pumps that are mounted next to the table in addition to a return tank that closes the flow loop. The shake table simulates earthquake motions with actuators that are controlled with feedback loop based on table displacement, which is measured with LVDTs, and frequencies up to 50 Hz can be input with accelerations up to 1.5 g.

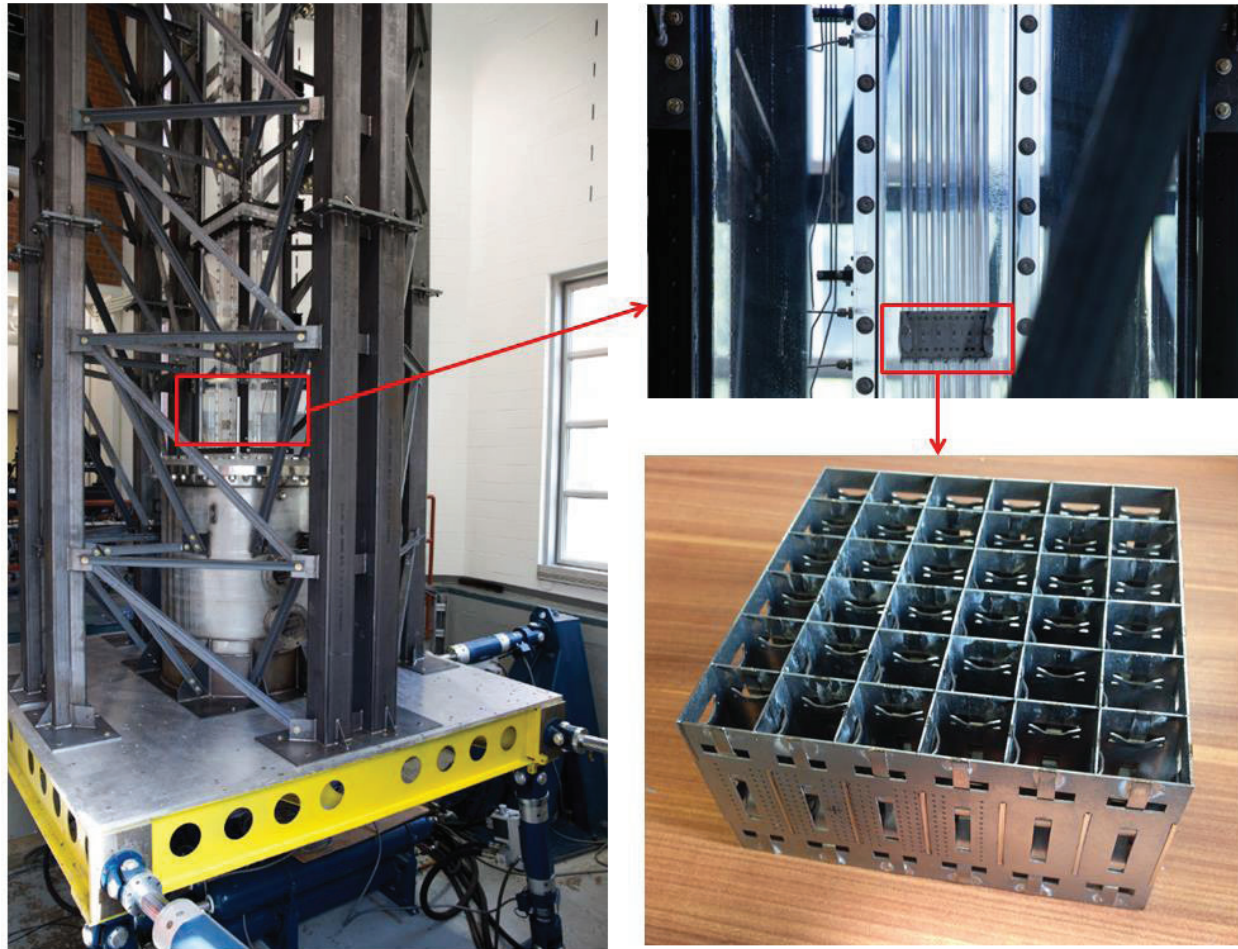


**Figure 7. Manufactured spacer grid and integration into experimental facility with SG-B highlighted**

## 5. MEASUREMENT TECHNIQUES AND RESULTS

The benefit of non-intrusive optical techniques in FSI measurements are that the instruments do not disturb the flow or add mass to the fuel assembly, which would alter resonant characteristics. However, it is challenging to take these measurements at a high spatial resolution that is needed to resolve these structural vibrations and flow features. In this facility this is accomplished by rigidly mounting all optics directly to the test section thereby taking measurements in the non-inertial, or moving, reference frame.

The optical techniques utilized for measuring the FSI coupling of the modal vibrations of the fuel assembly with that of the turbulent axial flow are DIC and PIV respectively. DIC is conducted with a multi-camera system in which a custom laser engraved pattern, Fig. 7, is tracked on each of the moving spacer grids with a pair of USB 3.0 cameras and pulsing LEDs, Fig. 8. The central four grids are tracked simultaneously and the cameras and LEDs are synchronized with a Berkley Nucleonics 575 time delay generator which has a 250 ps resolution, which both triggers the cameras and LEDs and controls the exposure time on the cameras and the pulse width on the LED. All these cameras record straight to hard drive and are time stamped by a high accuracy precision master clock that is essential for post-processing of the acquired data. This timestamp is also applied to five accelerometers that are located at different heights along the structure, as well as to the cameras used to record PIV. This allows for a reliable and

auditable method for synchronizing and integrating the collected data so that the measurements of external forcing from the accelerometers can be aligned with the modal response captured by DIC and the response of the fluid captured with PIV.

In Fig. 8 four raw images for each of the moving spacer grids captured with the DIC system are shown stacked on top of each other. The cross at the center of each image is tracked from one frame to the next, resulting in displacement values at 5-micrometer accuracy for the displacement of each spacer grid. A cross-correlation algorithm tracks the pattern between adjacent frames and, hence, reconstructs the displacements with resolution mentioned above. A manuscript is in preparation to describe this methodology in greater details.

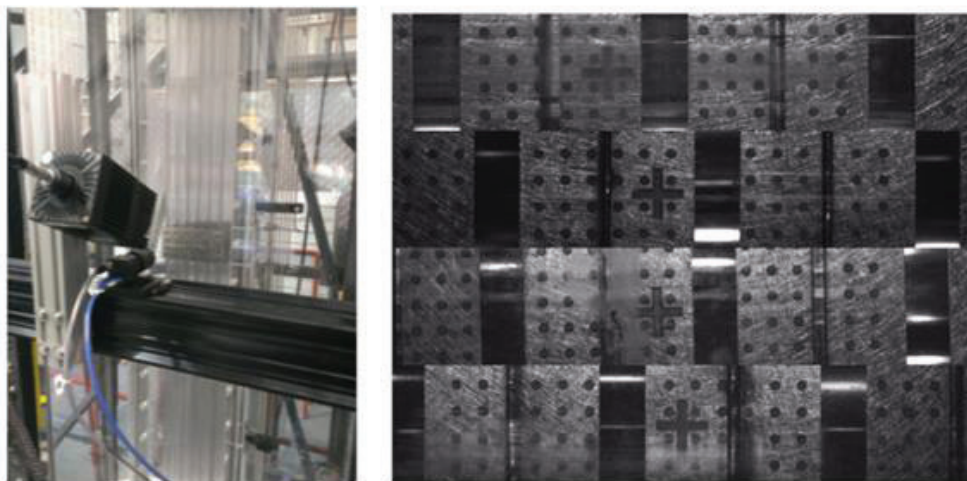


**Figure 8. Tracking between frames for one spacer grid and results from one spacer grid for sweeping frequency**

Results from the DIC post processing algorithm are seen in Fig. 9, where a sweeping frequency test is conducted with the shake table to excite the fuel assembly in air. In this test the shake table is set to run with a 1-D forcing at a fixed amplitude displacement of 1.5 mm, and a frequency sweep from 0.01 Hz to 6 Hz was programmed with a 0.01 Hz increment with one cycle completed for each frequency increment resulting in a total of 600 cycles. In prior experimental trials in air, it has been found that the first mode for the surrogate fuel bundle was 2 Hz and the second mode at 5.6 Hz. The sweeping test helps to confirm this, while it also portrays an asymmetric displacement of the fuel assembly that is attributed to the current spacer grid design as explained in following paragraph.

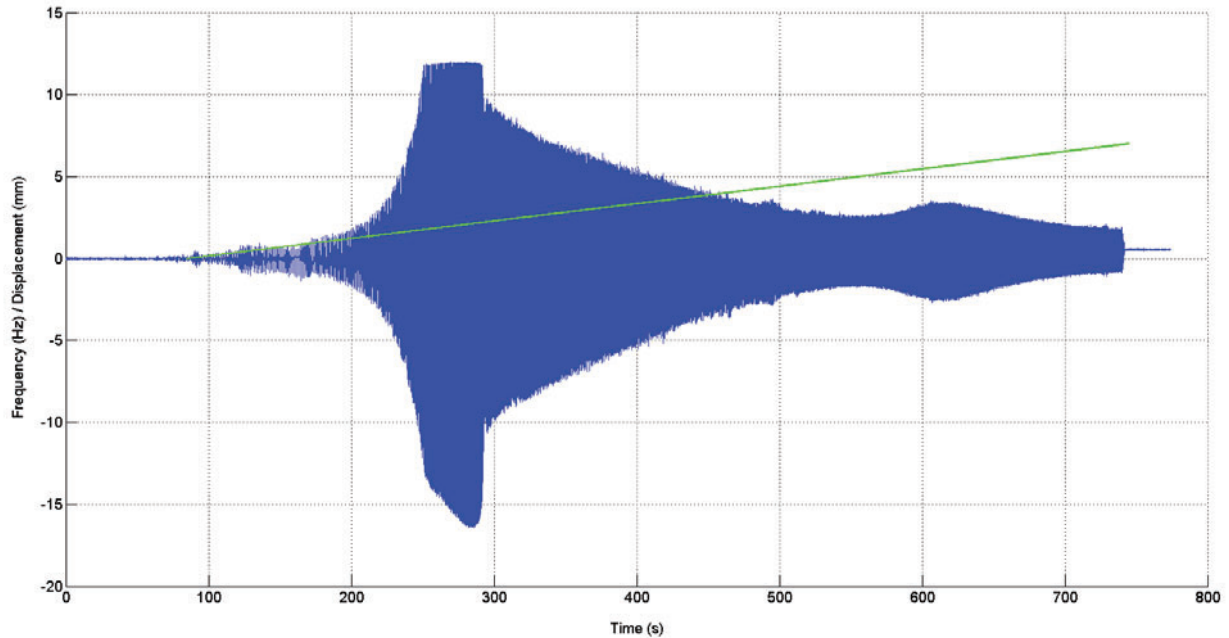


**Figure 9. Results from one spacer grid for sweeping frequency**

The inner acrylic channel that the fuel assembly is mounted in, has a bypass around the fuel assembly of  $1/4 P$  (5mm) in the non-forcing direction and  $1 P$  in the forcing direction (20 mm). The amplitude of the deflections, Fig. 9, do not exceed this bypass in either the positive or negative direction, so the plateau near the first mode in the positive displacement direction are due to a characteristic of the spacer grid with an asymmetric design. Relating Fig.2 to Fig. 9, when the fuel assembly moves to a positive amplitude it is towards the spring in the spacer grid, and when the fuel assembly moves to the negative side it is towards the dimple. It is believed that the surrogate fuel rods at first mode resonance are fully compressing the spring and making contact with the inner wall of the strap on the respective side resulting in the plateau seen in Fig. 9. This will be confirmed in future tests.

For tests with flow, a flying time-resolved PIV system has been developed to measure the fluid response. The laser sheet is delivered to a fixed region of the test section without beam wandering as a result of utilization of high-power fiber optics. Additionally, high speed cameras with a high magnification lens are mounted to the test section as well, Fig. 10 [17]. Similar to the cameras used for DIC, this camera also records straight to hard drive, and both the laser and camera are controlled by the time delay generator and monitored with an oscilloscope to ensure there is no overlap between the PIV and DIC measurements.

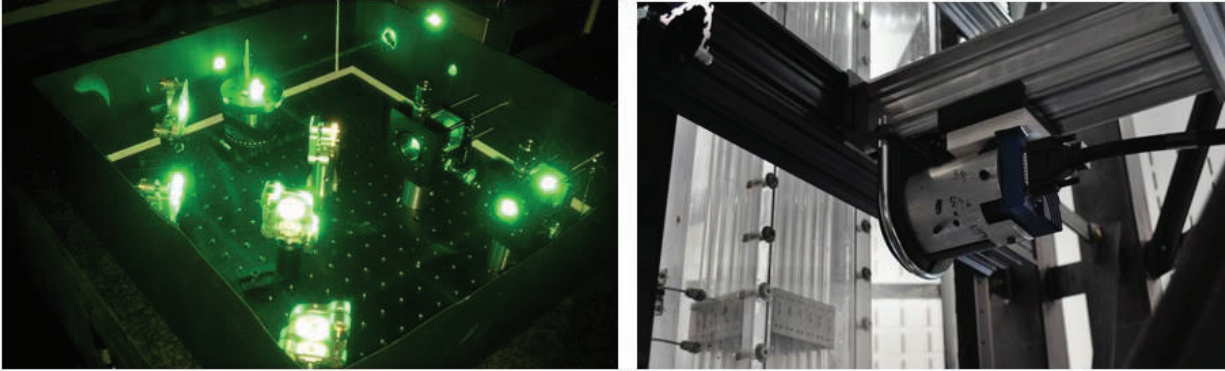


**Figure 10. Delivery of laser light with high powered multi-mode step index fiber optics and 4 Mpixel camera that records straight to hard drive**

In Fig. 11, static measurements are taken in a plane 75 mm above the first spacer grid between two of the acrylic rods at a high magnification ( $M = 1.6$ ). The laser and camera are both set at 5 kHz and 4096 raw PIV images are processed in DaVis version 8.2.2 in a time-series manner. A multi-pass interrogation method is utilized with a window starting at  $128 \times 128$  with a 50% overlap. Four passes are conducted, with the final window size being  $32 \times 32$  pixels with 75% overlap resulting in  $60 \times 100$  vectors per frame with a spatial spacing of 0.11 mm between vectors. Further measurements are planned just above the spacer grid and at varying locations between rods along the span of the spacer grid.

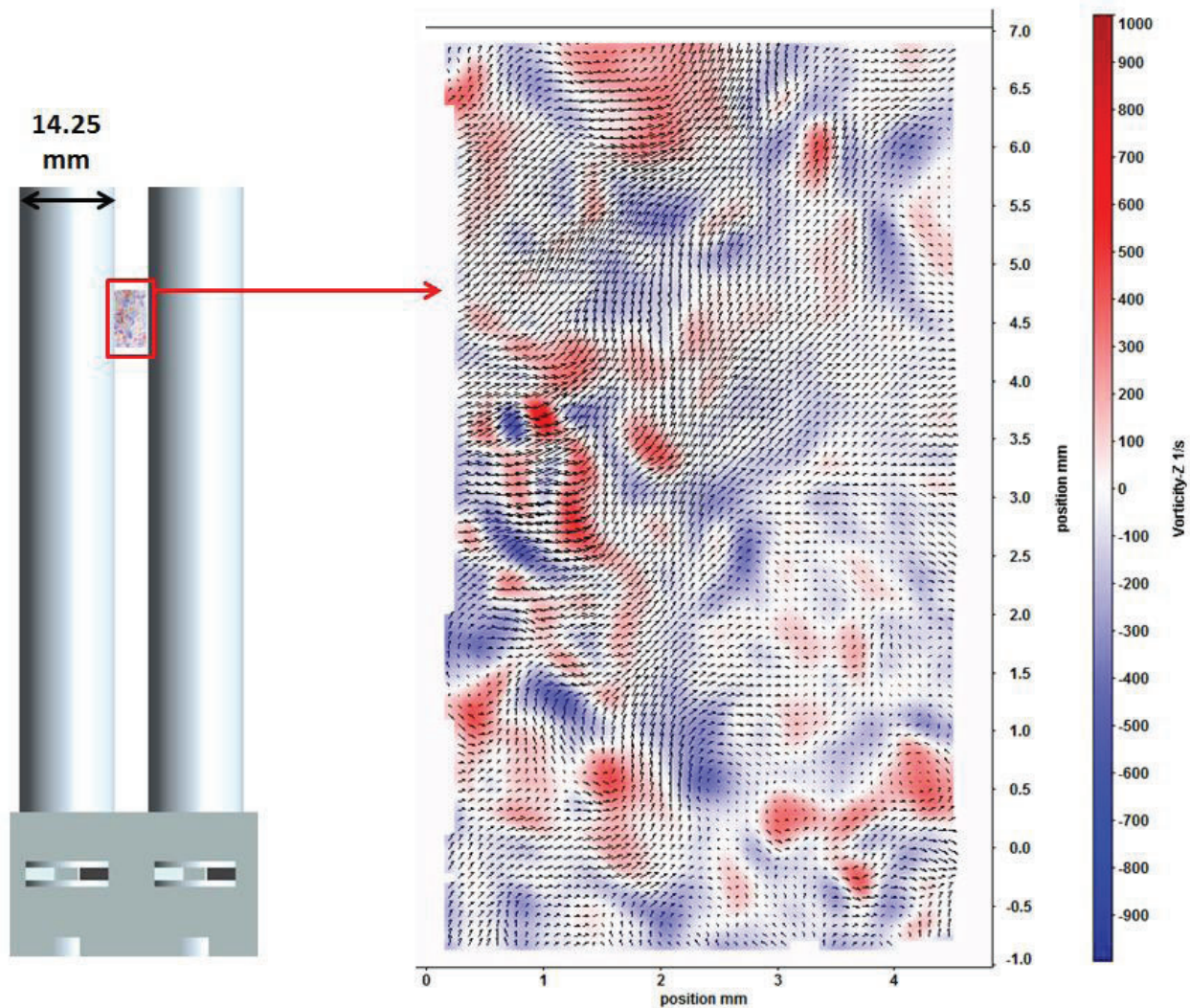


Figure 11. Instantaneous velocity field with vorticity in background

## 6. CONCLUSIONS

A methodology for the design and manufacture of a scaled spacer grid for flow induced vibrations studies with surrogate materials for use in a rod bundle has been outlined along with non-intrusive measurement techniques that can capture the FSI that occurs in a PWR core during seismic or large break LOCA forcing. Tests in air have shown similar results to an experimental setup at the Laboratory of Core and Circuit Hydrodynamics in France, where they conduct similar tests on a full scale PWR fuel assembly [16]. At this facility they excite the bundle with a hydraulic jack that is rigidly connected to one of the intermediate spacer grids. Further tests are planned to confirm observations made of the behavior of the spacer grids to seismic forcing in air, as well as additional tests in stagnant and moving fluid.

## REFERENCES

1. M.V. HOLLOWAY, "Fluid Dynamics and Heat Transfer of Turbulent Flow in Rod Bundle Subchannels," PhD Thesis (2005).

2. E.E. DOMINGUEZ-ONTIVEROS and Y.A. HASSAN, "Non-intrusive Experimental Investigation of Flow Behavior Inside a 5 x 5 Rod Bundle with Spacer Grids Using PIV and MIR," *Nuclear Engineering and Design*, 239, p. 888 (2009).
3. Hussain, S., Weichselbaum, N., Bardet, P., Cost Effective and Efficient Digital Image Correlation Sensors for Monitoring Vibration of Fuel Bundles
4. S.J. HAAM, R.S. BRODKEY, I. FORT, L. KLABOCH, M. PLACNIK, V. VANECEK, "Laser Doppler Anemometry Measurements in an Index of Refraction Matched Column in the Presence of Dispersed Beads Part I," *International Journal of Multiphase Flow*, 26, p. 1401 (1997).
5. Y.A. HASSAN, E.E. DOMINGUEZ-ONTIVEROS, "Flow Visualization in a Pebble Bed Reactor Experiment using PIV and Refractive Index Matching Techniques," *Nuclear Engr. and Design*, 238, p. 3080 (2008).
6. P.M. BARDET, C.D. FU, C.E. SICKEL, N.A. WEICHSELBAUM, "Refractive Index and Solubility Control of Para-cymene Solutions," 17<sup>th</sup> Int. Symp. On Applications of Laser Tech. for Fluid Mech (2014).
7. N.A. WEICHSELBAUM, M. ABKENAR, M. Vanella, M.T. Manzari, E. Balaras, P.M. Bardet, "Validation Data and Model Development for Nuclear Fuel Assembly Response to Seismic Loading," Proceedings of the ASME 2014 International Mechanical Engineering Congress & Expo (2014).
8. A. RUBIN, A. SCHOEDEL, M. AVRAMOVA, H. UTSUNO, S. BAJOREK, A. VELAZQUEZ-LOZADA, "OECD/NRC Benchmark Based on NUPEC PWR Subchannel and Bundle Tests (PSBT)," NEA/NSC/DOC(2010)1.
9. H.S. KANG, K.N. SONG, H.K. KIM, K.H. YOON, Y.H. JUNG, "Verification Test and Model Updating for a Nuclear Fuel Rod with its Supporting Structure," *Journal of the Korean Nuclear Society*, 33, p. 73 (2001).
10. B.L. SMITH, C.H. SONG, S.K. CHANG, J.R. LEE, J.W. KIM, "Report of the OECD/NEA-KAERI Rod Bundle CFD Benchmark Exercise," NEA/CSNI/R (2013).
11. N.E. TODREAS, M.S. KAZIMI, *Nuclear Systems I*, Taylor and Francis Group, New York, NY (1990)
12. K.J. PARK, B.S. KANG, K.N. SONG, G.J. PARK, "Design of a Spacer Grid using Axiomatic Design," *Journal of Nuclear Science and Technology*, 40, p. 989 (2003).
13. JCGM 100:2008, *Evaluation of measurement data - guide to the expression of uncertainty in measurement* (2008).
14. AISC, *Manual of Steel Construction Allowable Stress Design*, Chicago, IL
15. K. SONG, S. KIM, "Determination of the Optimum Welding Parameters for a Laser Welded Spacer Grid Assembly for PWRs," *Journal of Laser Micro/Nanoengineering*, 2, p. 95 (2007).
16. G. RICCIARDI, E. BOCCACCIO, "Stiffening of a Fuel Assembly Under Axial Flow," 10<sup>th</sup> International Conference on Flow Induced Vibration (2012).
17. N.A. WEICHSELBAUM, S. CLEMENT, S. WANG, M.A. ANDRE, M.R. ABKENAR, M. MANZARI, P.M. BARDET, "Single Camera PIV/Shadowgraphy and Laser Delivery on Earthquake Shake Table for Fluid-Structure Interaction measurements," 17<sup>th</sup> Int. Symp. On Applications of Laser Tech. for Fluid Mech (2014).